Dalton Transactions

ROYAL SOCIETY OF CHEMISTRY

PAPER

View Article Online
View Journal | View Issue

Cite this: *Dalton Trans.*, 2025, **54**, 17507

Plasma-enhanced atomic layer deposition of $AlPO_4/AlP_xO_y$: comparing dual source and supercycle approaches for composition control

Florian Preischel, [a,b] David Zanders, [a] Jean-Pierre Glauber, [a,b] Karl Rönnby, [c] Detlef Rogalla, [d] Thomas Gemming, [b] Peter Dement, [b] Michal Nolan [c] and Anjana Devi *[a,b,e,f]

In pursuit of developing a plasma-enhanced atomic layer deposition (PEALD) process for $AlPO_4$, we explored two different approaches, both employing an O_2 plasma as the co-reactant. First-principles density functional theory (DFT) calculations indicate that TMA-phosphine adducts are stable, with ethyl or isopropyl groups on the phosphine. The adducts were thermally characterized, with the newly synthesized $[Me_3AlP^iPr_3]$ (**TMAPIP**) featuring a promising one-step evaporation. Therefore, it was tested as a dual-source precursor at 120 °C, providing both Al and P atoms for the resulting AlP_xO_y layers, thereby simplifying the process design. Although the P content of the PEALD-deposited films was limited to a few percent, this might be advantageous for P doping of Al_2O_3. The second approach, therefore, involved a supercycle (SC) process design, in which the number of phosphorus reagent sub-cycles using $P(NMe_2)_3$ as the precursor was varied alongside a single Al_2O_3 cycle with TMA; in both cases, O_2 plasma was used as the co-reactant. Simple gas-phase DFT calculations show that $P(NMe_2)_3$ reacts favorably with the chemisorbed Al species present in the second sub-cycle. The SC method enabled the incorporation of significantly higher amounts of P over a broad temperature range from 60 °C to 240 °C. The deposition of stoichiometric $AlPO_4$ was ultimately achieved by varying the number of phosphorus cycles, allowing the composition to be precisely adjusted *via* the deposition temperature.

Received 23rd September 2025,
Accepted 30th October 2025

DOI: 10.1039/d5dt02282g

rsc.li/dalton

Introduction

Aluminum phosphate ($AlPO_4$) naturally occurs as the mineral berlinite and has diverse industrial applications.[1] It exhibits good mechanical strength, chemical resistance, as well as high temperature stability with a melting point of 1800 °C, featuring a microporous framework structure composed of interconnected PO_4 and AlO_4 tetrahedra.[1–4] This structure makes it particularly interesting as a molecular sieve.[5,6] As a thin film, $AlPO_4$ is applied to enhance the electrochemical performance and stability of cathode materials for lithium-ion batteries,[7–9] as an oxidation-resistant coating for carbonaceous materials.[10–12] Owing to its wide bandgap (6.0 eV for the hexagonal phase)[13] and moderate permittivity of approximately 5, which can be enhanced by inclusion of dopants, it is investigated as a gate dielectric.[14] However, a significant limitation arises for high-temperature applications: stoichiometric, crystalline $AlPO_4$ undergoes polymorphic transformations, which can already occur below 200 °C (ref. 15) and go along with considerable volume changes and alterations in functional properties upon heating.[3,16,17] This can be avoided by employing non-stoichiometric, amorphous AlP_xO_y, which has been reported to be particularly temperature stable, enabling applications exceeding 1000 °C.[16,18] Additionally, a dense, amorphous structure is preferred for protective coatings, as polycrystalline materials feature grain boundaries that serve as diffusion pathways, limiting the effectiveness of the protective layer.[19–21] Consequently, controlling the composition, particularly the phosphorus-to-aluminum (P/Al) ratio, and the structure of the deposited material becomes critical to ensure performance and tailor functional properties. For example, Hornsveld *et al.* demonstrated that the stoichiometry of AlP_xO_y can be used to tune its refractive index.[22] Further, these thin-film applications necessitate uniform, conformal, and closed coatings on 3D structures, including high-surface-area powders, with precise thickness control on the nanometer scale. Atomic layer depo-

[a]*Inorganic Materials Chemistry, Ruhr University Bochum, Universitätsstr. 150, 44801 Bochum, Germany*
[b]*Leibniz Institute for Solid State and Materials Research, Helmholtzstr. 20, 01069 Dresden, Germany. E-mail: a.devi@ifw-dresden.de*
[c]*Tyndall National Institute, Lee Maltings, University College Cork, Cork T12 R5CP, Ireland*
[d]*RUBION, Ruhr University Bochum, Universitätsstr. 150, 44801 Bochum, Germany*
[e]*Fraunhofer Institute for Microelectronic Circuits and Systems (IMS), Finkenstr. 61, Duisburg, Germany*
[f]*Chair of Materials Chemistry, TU Dresden, Bergstr. 66, 01069 Dresden, Germany*

sition (ALD) effectively addresses these challenges by enabling scalable deposition of conformal thin films with clearly defined interfaces and precise thickness control under relatively mild process conditions.[23,24] Specifically, plasma-enhanced ALD (PEALD) further enhances deposition capabilities by enabling lower deposition temperatures and introducing the plasma as an additional parameter to influence the materials' composition and properties.[25,26] Recently, a stable two-dimensional (2D) bilayer form of $AlPO_4$ has been proposed by theoretical studies.[27] This bilayer structure is characterized by the absence of covalent bonds to the surface and features intrinsic pores, which could enable its use as a size-selective gas separation membrane. We previously demonstrated the feasibility of creating 2D silica membrane structures by PEALD and showed that precisely controlling the amount of deposited material is crucial for achieving the 2D form.[28,29] Therefore, the mechanical and chemical stability of $AlPO_4$ is beneficial for fabricating a membrane that withstands harsh operating conditions, but comparable experimental research on $AlPO_4$ is lacking. Therefore, this study aims to provide an experimental basis for the development of 2D $AlPO_4$ by establishing a suitable PEALD process, conducting detailed investigations of the process parameters, and performing initial downscaling experiments.

Early demonstrations of $AlPO_4$ ALD relied on $AlCl_3$ or [Al(O^nPr)$_3$] combined with P_2O_5 or trimethylphosphate ($PO(OMe)_3$, TMPO) and water or *tert*-butanol. Still, they required temperatures of at least 450 °C with undesirable chlorine impurities, in the case of $AlCl_3$.[30,31] Subsequently, Hämäläinen *et al.* directly reacted $AlCl_3$ with TMPO, without the use of an additional co-reactant, at temperatures ranging from 150 °C to 400 °C.[32] Knohl *et al.* followed the same route with triethylphosphate ($PO(OEt)_3$) at 250 °C.[10] However, the amount of P incorporated with this approach is limited, resulting in significantly P-deficient material. As an alternative precursor, Kvamme *et al.* employed trimethylaluminum (TMA) and H_2O in supercycles (SCs) with trimethylhosphite ($P(OMe)_3$) and H_2O between 175 °C and 275 °C. In such an SC process, two binary ALD cycles are alternated to synthesize a multicomponent thin film.[33] Yet, the incorporation of P was limited, and films featured P/Al ratios below 0.2.[34] Recently, PEALD processes were shown to mitigate this limitation by using O_2 plasma as the co-reactant, enabling near-stoichiometric $AlPO_4$ compositions. While Dobbelaere *et al.* followed a three-step process of TMPO plasma polymerization, O_2 plasma, and TMA exposure,[35] Hornsveld *et al.* employed an SC sequence of TMA and TMPO individually reacted with O_2 plasma.[22] The TMPO plasma step employed by Dobbelare *et al.* resulted in CVD-like reactions at temperatures below 300 °C. In contrast, the SC approach by Hornsveld *et al.* was feasible from 25 °C to 300 °C, allowing control over the composition by adjusting the number of PO_x cycles. Lately, tris-dimethyl-aminophosphate ($P(NMe_2)_3$) has emerged as an alternative reactive phosphorus source in ALD of slightly P-deficient MgP_xO_y thin films.[36] Most recently, Blomme and co-workers adopted $P(NMe_2)_3$ for PEALD of AlP_xO_y, yielding P/Al ratios of up to 1.66 when reacted with O_2 plasma and alternated in supercycles with TMA and O_2 plasma between 125 °C and 350 °C.[37] These studies demonstrate the potential of $P(NMe_2)_3$ for the deposition of phosphate materials, specifically in plasma processes, which motivated its selection as the phosphorus reactant for the SC PEALD process in this study.

On the other hand, in metal–organic chemical vapor deposition (MOCVD), single-source precursors are available that include both the metal and its binding partner for the deposited material; therefore, a co-reactant is not necessary.[38,39] This approach can simplify the process design and has also been tested for MOCVD of $AlPO_4$.[40] Due to the cyclic procedure of ALD, where the precursor and co-reactant are necessarily introduced separately, it is not possible to use this approach for ALD of binary materials. When depositing ternary materials, however, one can design a "single source" precursor that bears two of the materials' constituents in the desired stoichiometry[33] and is thus labelled a dual source precursor in the following. Such an approach has been evaluated previously, *e.g.*, for $NdAlO_x$ [41] and various silicates.[42–44] To realize this ALD method for $AlPO_4$, a precursor that contains both Al and P must be designed and subsequently reacted with an oxygen source. To achieve this, we have investigated TMA complexes with phosphorus adducts, namely triethylphosphine (PET) and triisopropylphosphine (PIP). The Al metal in TMA is highly electron-deficient and therefore acts as a strong Lewis acid, forming a dimeric species in its pure form.[45,46] P^{3+} compounds, on the other hand, act as Lewis bases, due to the free electron pair at the P center. Hence, these compounds readily donate their free electron pair to TMA, resulting in the complexes trimethylaluminum triethylphosphine, [Me_3AlPEt_3] (**TMAPET**), and trimethylaluminum triisopropylphosphine, [$Me_3AlP^iPr_3$] (**TMAPIP**). While the synthesis of **TMAPET** has been reported previously,[47,48] **TMAPIP** has been described only theoretically[49] and both complexes have not been thermally characterized. With these adducts, the Al center is electronically saturated and sterically shielded, thereby increasing stability relative to TMA while still imparting sufficient reactivity for ALD. This approach could also help monomerize the resulting complexes,[50,51] which is generally beneficial for ALD applications as it results in a more predictable evaporation and reaction behavior. When employing **TMAPIP** in PEALD, the achievable P content is limited; however, this approach enables the deposition of intrinsically and uniformly P-doped Al_2O_3 for controlled material tuning.[30,52,53] Motivated by the results from Blomme *et al.*,[37] we alternatively investigated a SC sequence with separate PO_x and Al_2O_3 PEALD cycles, using $P(NMe_2)_3$ and TMA with O_2 plasma to enhance the P content in the films. The composition of the films resulting from the SCs can be readily tuned by varying the number of PO_x cycles in conjunction with the deposition temperature, and by choosing appropriate parameters, stoichiometric $AlPO_4$ is obtained.

Results and discussion

Synthesis and characterization of TMA-phosphine adducts

The synthesis of **TMAPET** and **TMAPIP** proceeds in a straightforward way by dissolving the respective phosphine in diethyl

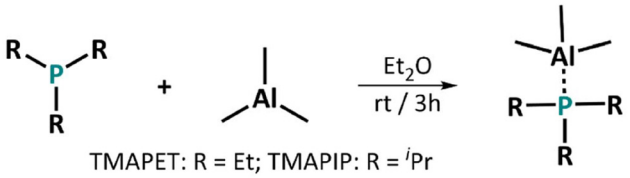

Scheme 1 Synthesis of the TMA-phosphine adducts **TMAPET** (R = Et) and **TMAPIP** (R = iPr) with a stirring time of 3 hours at room temperature (rt).

ether (Et_2O) and adding TMA, as depicted in Scheme 1. After stirring the mixture and removing the solvent, the target complexes can be isolated in almost quantitative yields above 90%. **TMAPET** was obtained as a colorless liquid by distillation at 60 °C, and **TMAPIP** as a colorless solid by sublimation at 68 °C under reduced pressure. The fact that the compounds can be obtained by distillation/sublimation at moderate temperatures is already a strong indication of their volatility and that they can be transported in the gas phase.

The obtained compounds were analyzed by ^{1}H NMR (Fig. 1) to verify their structure and purity. The full spectra are given in Fig. S1, alongside the respective ^{13}C spectra. In organophosphorus compounds, coupling of ^{1}H and ^{13}C to ^{31}P can be observed in addition to J_{HH} coupling, whereby the coupling constantly decreases with the number of bonds between the respective coupling partners.[54,55] Accordingly, peaks A and B in the ^{1}H NMR spectrum can be clearly assigned to the phosphorus adduct of each complex.

The coupling patterns are shown in detail by a magnified view of the regions of interest in Fig. S2 in the SI. For **TMAPIP**, the protons of the CH groups appear as a doublet of quartets (peak A, 1.73 ppm, 3H, J = 14.5, 7.3 Hz) due to $^2J_{HP}$ coupling, and the CH_3 protons from the isopropyl groups appear as a doublet of doublets with $^3J_{HP}$ coupling (0.91 ppm, 18H, J = 13.2, 7.2 Hz). For **TMAPET**, peak A corresponds to the protons of the CH_2 groups and B to those of the CH_3 groups from the ethyl chains (1.03 ppm with 6H and 0.71 ppm with 9H, respectively). Both appear as complex (and rather poorly resolved) multiplets. This is likely because the ethyl chains can freely rotate, averaging the dihedral angles and diminishing the observable splitting, unlike the rigid isopropyl groups in **TMAPIP**. Lastly, the protons of the CH_3 groups bonded directly to the electropositive Al center are accordingly high-field shifted and appear as a singlet at −0.33 ppm and −0.26 ppm for **TMAPET** and **TMAPIP**, respectively (peak C, 9H), whereas the respective protons of pure TMA appear at −0.18 ppm.[56] The shift of this signal thus not only verifies the bonding of the P-adducts to the Al center but also reflects the influence of the different phosphines on the electronic structure of the adducted TMA.

Additionally, the ^{13}C NMR spectra (Fig. S1) show three peaks (a, b, and c) corresponding to the three distinct carbon atoms in each complex. For **TMAPET**, peak a can be assigned to the CH_2 carbons, and for **TMAPIP** to the carbons of the CH groups (13.35 ppm and 20.89 ppm, respectively). The CH_3 carbons from the ethyl- and isopropyl groups appear at 7.55 ppm for **TMAPET** and at 19.12 ppm for **TMAPIP** (peak b). Additionally, coupling between ^{13}C and ^{31}P can be observed for the carbon atoms of the phosphorus adducts (see Fig. S2 for a magnified depiction). For both complexes, peak a appears as a doublet, due to $^1J_{CP}$ coupling, while the $^2J_{CP}$ coupling is weaker and only properly resolved for peak b of **TMAPIP**. The difference in the J_{CP} coupling strength of **TMAPET** and **TMAPIP** can likely be explained in the same way as for the J_{HP} coupling: the ethyl groups can rotate freely, which reduces the splitting compared to the rigid isopropyl groups. The carbons from the TMA moiety appear as a broad signal (peak c) that is high-field shifted to −8.21 ppm for **TMAPET** and to −5.92 ppm for **TMAPIP** due to the shielding effect of the electron density drawn from the electropositive Al.

The purity of the as-obtained $P(NMe_2)_3$ was confirmed by ^{1}H NMR (Fig. S3), and as expected, only one signal is detected

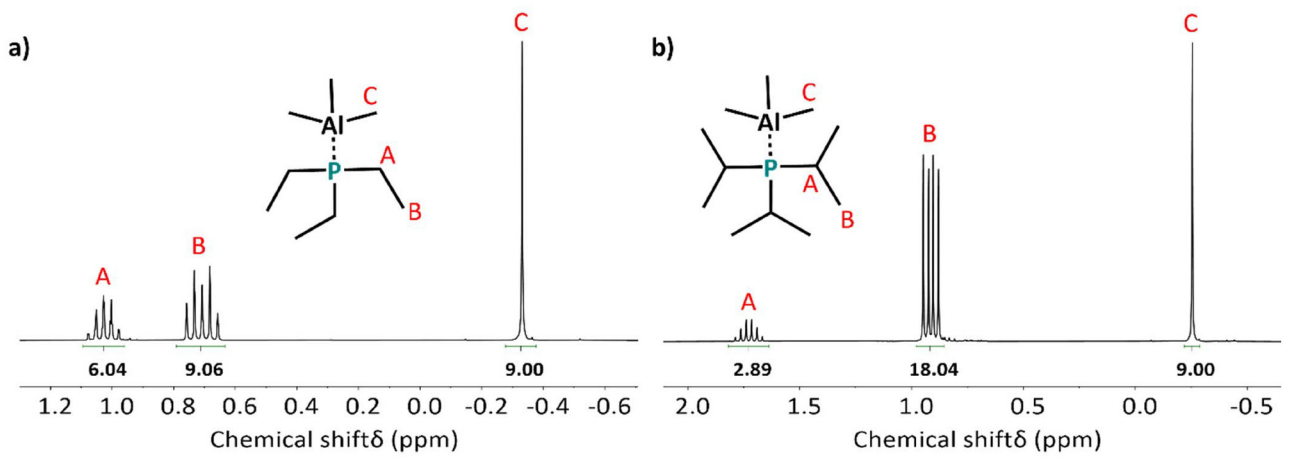

Fig. 1 ^{1}H NMR of (a) **TMAPET** and (b) **TMAPIP** in benzene-d_6 with a zoom into the region with the product peaks.

that corresponds to the CH_3 protons of the amide groups. This signal appears as a doublet (J = 9.0 Hz) at 2.48 ppm, due to $^3J_{HP}$ coupling.

The structures and stabilities of the TMA-phosphine adducts were investigated using density functional theory (DFT). Both **TMAPET** and **TMAPIP** complexes relax to similar structures, with the Al and P centers adopting tetramer configurations, as depicted in Fig. 2. The Al–P bond is 2.525 Å in **TMAPET** and 2.550 Å in **TMAPIP**, indicating that the effect of the bulkier isopropyl ligands on the binding to Al in the adduct is negligible. Upon forming the adduct, the Al–C bonds elongate slightly from 1.960 Å in TMA to 1.990 Å in both **TMAPET** and **TMAPIP**, while the P–C bonds shrink slightly from 1.850 Å in PET to 1.833 Å in **TMAPET** and from 1.874 Å in PIP to 1.858 Å in **TMAPIP**. Overall, these results are in good agreement with those reported by Kuczkowski *et al.*, except that their previously reported Al–P bond lengths are slightly longer, with 2.661 Å for **TMAPET** and 2.694 Å for **TMAPIP**.[49] The adduct formation is exothermic for both adducts, with computed formation energies of −83 kJ mol^{-1} for **TMAPET** and −82 kJ mol^{-1} for **TMAPIP**. This further confirms that the size of the ligands on phosphorus has a minimal effect on the structural stability of the adducts. Still, the magnitude of the interaction energies suggests that the adduct species will be reactive for ALD chemistry.

Thermal evaluation of TMAPET, TMAPIP, and $P(NMe_2)_3$

To evaluate the suitability of **TMAPET** and **TMAPIP** as dual-source precursors for ALD of $AlPO_4$, their thermal behavior was analyzed by thermogravimetric analysis (TGA), alongside $P(NMe_2)_3$ as a potential precursor for a separate PO_x cycle (Fig. 3). To account for the air sensitivity of these complexes, the TG measurements were conducted under an inert N_2 atmosphere in a glove box. $P(NMe_2)_3$ exhibits a clean one-step evaporation with an onset temperature (1% mass loss) of 31 °C and a step-temperature of 93 °C. The evaporation step ends abruptly at 120 °C with no residual mass. This evaporation profile indicates that the compound can be readily evaporated and transported to a substrate at low temperatures, making it an ideal ALD precursor.

Among the P-adducts, **TMAPET** demonstrated higher volatility with an evaporation onset of 28 °C, consistent with its lower molecular mass. However, its evaporation occurs in three steps. The initial mass loss occurred until around 120 °C, leaving approximately 60% of the original mass. This closely matches the theoretical mass fraction (62%) for the PEt_3 fragment of the complex, suggesting that after a short initial evaporation period, TMA is released, leaving PEt_3 behind. The second step proceeds to approximately 213 °C, with a rest mass of 36%, beyond which the mass loss slows significantly. For PEt_3, a thermal decomposition temperature of 220 °C is documented.[57] Hence, it is plausible that the observed behavior is due to initial volatilization of PEt_3, which subsequently begins to thermally decompose upon reaching its thermal decomposition threshold. At higher temperatures, a gradual mass loss persists, reaching a final rest mass of 23%. While determining precise decomposition pathways would require additional mass spectrometric analysis of evolved gases, the TGA results clearly indicate that **TMAPET** undergoes facile thermal decomposition and possesses a limited effective volatilization window.

In contrast, **TMAPIP** exhibits one-step evaporation with an onset temperature of 55 °C and a step temperature of 153 °C. This demonstrates an improved stabilization effect of the PIP adduct, resulting in enhanced thermal stability despite similar bond energies calculated by DFT. This is presumably due to more effective steric shielding of the Al center by the bulkier isopropyl groups. This step is completed around 237 °C with a reduction in mass loss rate beyond 200 °C. The primary step leaves a residual mass of 13%, which slowly decreases further to 8% at the end of the measurement. This behavior indicates that **TMAPIP** initially evaporates intact and begins to decompose above 200 °C, leaving a non-volatile residue. Therefore, **TMAPIP** provides a sufficiently large temperature window for evaporation, spanning at least from its onset up to its step temperature, making it an appealing precursor for gas-phase deposition methods.

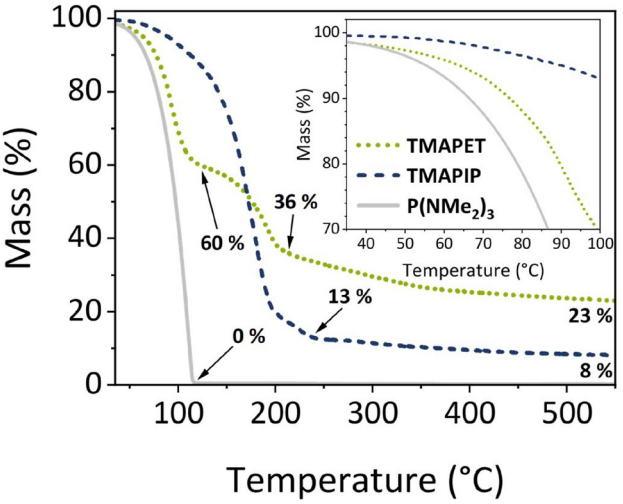

Fig. 3 TG curves of **TMAPET** (dotted green line), **TMAPIP** (dashed blue line), and $P(NMe_2)_3$ (grey line). The inset shows a magnified view of the evaporation onset.

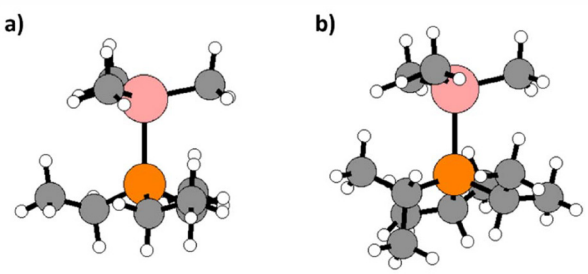

Fig. 2 DFT optimized structures of (a) **TMAPET** and (b) **TMAPIP**. Pink atoms are Al, orange P, grey C, and white H.

In addition, the vapor pressures of **TMAPET** and **TMAPIP** were estimated from differential TG (DTG) data, following established literature procedures.[58,59] Thereby, the Langmuir equation describes the vapor pressure–temperature correlation[60] and using Clausius–Clapeyron plots (Fig. S4), the temperature at which the compounds have a vapor pressure of 1 Torr ($T_{1\ \mathrm{Torr}}$) can be estimated. This figure of merit is often used to compare precursor volatility.[61] For **TMAPET** a $T_{1\ \mathrm{Torr}}$ of around 38 °C was determined and for **TMAPIP** one of around 68 °C. While this represents an increase compared to TMA ($T_{1\ \mathrm{Torr}}$ of −13 °C, as determined by McCullough and co-workers)[62] it is well below the step temperature of the respective complexes and suitable for typical gas-phase deposition applications (Table 1).

In conclusion, despite its lower volatility compared to **TMAPET**, **TMAPIP** emerges as the more promising precursor candidate because it volatilizes intact in a single step. The enhanced stability of **TMAPIP** is consistent with the higher Lewis basicity of P^iPr_3 compared to PEt_3 and its higher computed dissociation energy.[49] To further analyze the structure of **TMAPIP** in the gas phase, liquid injection field desorption ionization mass spectrometry (LIFDI-MS) was conducted, as depicted by a zoom on the $[M]^+$ region in Fig. 4 with the full spectrum shown in Fig. S5. Next to a signal at m/z = 92.05 corresponding to the solvent toluene, the spectrum shows the $[M + H]^+$ peak at m/z = 233.13 with the expected isotopic pattern due to the share of ^{13}C.

The formation of a protonated species during ionization process is known for LIFDI[63] and is facilitated by the Lewis basicity of the phosphine adduct. Further signals are observed at higher m/z ratios (Fig. S5), which could originate from dimerization and aggregation with alkali ions taken up from the glassware,[63,64] as well as from partial fragmentation of the ligands under the ionization conditions.

These results verify the attachment of the P adduct to TMA and show the presence of a monomeric species in the gas phase, rather than solely dimeric TMA. This demonstrates the proposed electronic and steric saturation of the Al center. With the described thermal and structural characteristics, **TMAPIP** should enable the simultaneous transport of Al and P to a substrate and therefore potentially act as a dual-source precursor that delivers two constituents of the ternary $AlPO_4$. This could simplify the process design by eliminating the need for separate ALD cycles that are typically required for ternary materials. Consequently, a PEALD process utilizing **TMAPIP** with O_2 plasma as the co-reactant was pursued to deposit $AlPO_4$ thin films.

Table 1 Thermal properties of **TMAPET**, **TMAPIP**, and $P(NMe_2)_3$ as derived from TGA

Thermal property	**TMAPET**	**TMAPIP**	$P(NMe_2)_3$
1% mass loss (°C)	28	55	31
Step temperature (°C)	80 (1st step)	153	93
Step completed (°C)	120; 213	237	120
Mass at end of step (%)	60; 36	13	0
Rest mass (%)	23	8	0
$T_{1\ \mathrm{Torr}}$ (°C)	38	67	—

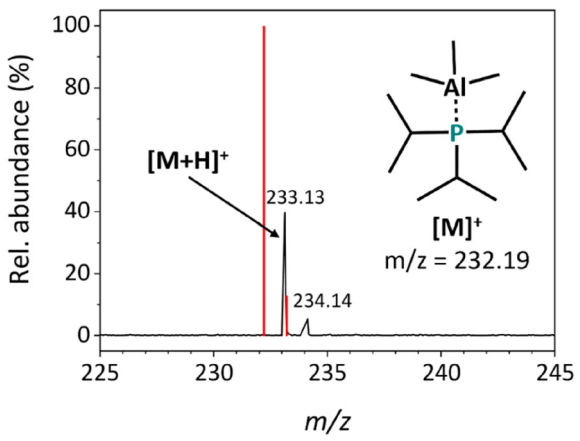

Fig. 4 LIFDI-MS spectrum of **TMAPIP** recorded in toluene with a zoom into the $[M]^+$ region. The red lines mark the expected $[M]^+$ isotope pattern.

Dual-source PEALD approach for AlP_xO_y

At a deposition temperature of 120 °C and a plasma pulse duration of 500 ms, saturation of **TMAPIP** was achieved with a pulse length of 1200 ms (Fig. 5a). The composition of the deposited films was analyzed by Rutherford backscattering spectrometry combined with nuclear reaction analysis (RBS/NRA). In RBS, heavier atoms are detected at higher energies due to conservation of momentum of the backscattered ions, causing the signal from the Si substrate to overlap with the O and Al signals, as well as potential C and N impurities, as can be seen in Fig. 5b. NRA can reliably determine the lighter elements (C, N, O), but quantification of the Al content necessitates deposition on alternative substrates. Glassy carbon (GC) was selected for this purpose due to its elemental composition, with C being the lightest element for which substrates are readily available. By depositing each film to be analyzed simultaneously on Si and GC, the AlP_xO_y composition was reliably determined (Fig. 5c). For better comparability, the stoichiometry of all investigated samples has been calculated by normalizing the P and O concentrations relative to Al, yielding the composition as $Al_1P_xO_y$, as listed in Table 2. Comprehensive compositional data obtained from both Si and GC are provided in the SI (Tables S1 and S2), showing that impurity-free films were obtained with C and N values within the error range or below the detection limit of RBS/NRA. Variation in plasma pulse duration from 150 ms to 500 ms had no apparent effect on the composition. P concentrations consistently remained below 4 at%, corresponding to an approximate composition of $AlP_{0.1}O_{2.0}$ (Table 2). Notably, the O concentration exceeded that expected for pure Al_2O_3, and samples with higher P levels concurrently exhibited higher O content. This observation suggests that the P is incorporated into the film lattice and chemically bonded to aluminum as Al–O–P species, rather

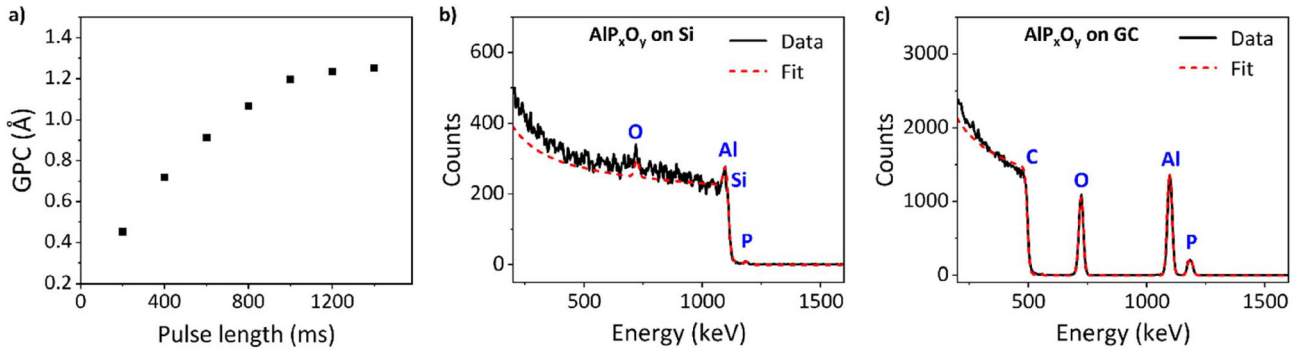

Fig. 5 (a) Saturation of **TMAPIP** in the PEALD process using 300 cycles. RBS spectra of AlP_xO_y deposited using **TMAPIP** on (b) Si and (c) GC.

Table 2 Stoichiometry of AlP_xO_y thin films deposited on GC at 120 °C using **TMAPIP** with varying O_2 plasma pulse length, determined from RBS/NRA results

O_2 plasma pulse (ms)	Al	P	O
150	1.00	0.11	2.05
300	1.00	0.10	2.01
500	1.00	0.12	2.14

than merely existing as an impurity within an Al_2O_3 matrix. Despite successful incorporation of P into the films, stoichiometric $AlPO_4$ formation appears infeasible with the dual-source precursor **TMAPIP**. The fact that the P content is significantly below the stoichiometric value for $AlPO_4$ suggests that this is an intrinsic flaw of the process. A possible explanation for this growth behavior is that **TMAPIP** chemisorbs to the surface by releasing the phosphine, thereby preventing the stochiometric incorporation of P. Yet, the dual-source approach allows for deposition of Al_2O_3 intrinsically doped with up to several at% of P. To elucidate the chemisorption mechanism, *in situ* analysis, such as X-ray photoelectron spectroscopy (XPS) of the growing film or MS of the exhaust gases, could be performed in future studies aimed at precise control over the P-content.

As the dual-source approach did not yield the desired results, we established a SC approach using intermittent cycles of a separate phosphorus precursor and TMA, both with O_2 plasma as the co-reactant. A similar approach has recently been reported and analyzed in detail by Kessels *et al.* using PO$(OMe)_3$ as the phosphorus precursor with O_2 plasma,[22] while Rosowski *et al.* employed $P(NMe_2)_3$ with H_2O in an application-focused study without reporting details of the ALD process.[65] Very recently, Blomme *et al.* built upon this study by investigating different sequences of TMA, $P(NMe_2)_3$, and H_2O or O_2 plasma between 125 °C and 350 °C.[37]

Inspired by these studies, we used the highly volatile $P(NMe_2)_3$ as the phosphor precursor for PEALD to provide a deeper understanding of the process, particularly the effects of the SC scheme on the composition of deposited films, focusing on low-temperature depositions.

$AlPO_4$ supercycle approach: $P(NMe_2)_3$ and TMA with O_2 plasma

To study the ALD reactivity of $P(NMe_2)_3$, we explored a simplified gas-phase model in which the precursor interacts with Al$(OH)_3$, which describes the reactive surface species after the TMA + O_2 plasma step. Upon reaction, a hydrogen atom is transferred from one of the hydroxyl groups at Al$(OH)_3$ to one of the $–NMe_2$ groups, which is released as $HNMe_2$. A new bond is formed between the P and O atoms, with a P–O distance of 1.588 Å. Additionally, the Al atom engages in coordinative bonding with a N in one of the remaining $–NMe_2$ groups, forming a tetrahedral complex with an Al–N distance of 1.985 Å (Fig. 6). The reaction is moderately exothermic with a reaction energy of −126 kJ mol^{-1}, showing that the proposed ALD reaction is favorable.

Initially, one PO_x cycle (referred to as A sub-cycle in the following), consisting of a $P(NMe_2)_3$ pulse and O_2 plasma exposure, was combined with one Al_2O_3 cycle (B sub-cycle) of TMA pulse and O_2 plasma exposure. The TMA cycle was adapted from a prior study in the same reactor,[66] and the complete scheme is depicted as an inset in Fig. 7.

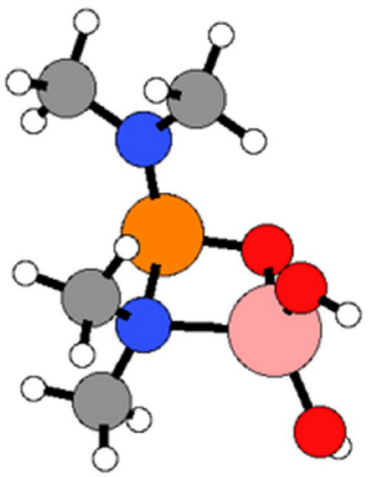

Fig. 6 DFT relaxed product after reaction between $P(NMe_2)_3$ and Al$(OH)_3$. The pink atom is Al, and orange is P; grey atoms are C, red O, blue N, and white H.

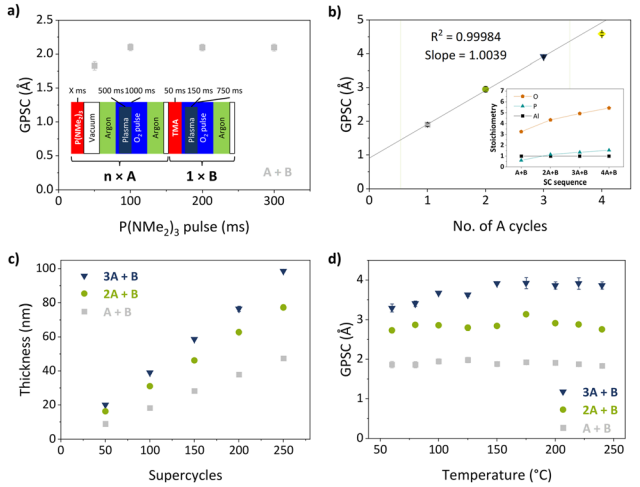

Fig. 7 PEALD process development for AlP_xO_y thin films using $P(NMe_2)_3$ and TMA in a supercycle with O_2 plasma on Si. (a) Saturation of the $P(NMe_2)_3$ pulse at 150 °C with a scheme of the supercycle as an inset. (b) GPSC with different SC sequences at 150 °C. As an inset, the stoichiometry of the resulting thin films on GC is shown, as determined by RBS/NRA on GC. P and O values have been normalized to an Al ratio of 1. (c) Linearity of thickness *vs.* the number of applied supercycles for different SC sequences. (d) Temperature dependency of the SC sequences.

With a deposition temperature (T_{dep}) of 150 °C and plasma duration of 500 ms, the $P(NMe_2)_3$ pulse length was varied. Except for the linearity, all depicted depositions have been carried out with 150 supercycles (SCs). As shown in Fig. 7a, saturation was achieved from 100 ms onward, with a growth per SC (GPSC) of 2.1 Å, demonstrating the self-limiting behavior of the P-cycle.

As demonstrated by Hornsveld *et al.*,[22] the P content in the films can most effectively be controlled by the number of P-cycles. Consequently, we investigated different supercycle schemes with varying numbers of P-cycles before each Al-cycle at 150 °C. From 1 to 3A sub-cycles, the GPSC increased linearly but slightly flattened with 4A, as demonstrated by an extension of a linear fit of the first three data points in Fig. 7b. It seems that the amount of material deposited by the PO_x cycles begins to slow down when more than three consecutive A cycles are employed before introducing new Al-sites with a B cycle. This is in line with the observation of saturation after a few PEALD cycles of only $P(NMe_2)_3$ with O_2 plasma by Blomme *et al.*[37]

As observed for **TMAPIP**, RBS/NRA showed that all films deposited with $P(NMe_2)_3$ and TMA are impurity-free. Further analysis of the composition revealed P- and O-deprived $AlP_{0.60}O_{3.25}$ films for the A + B sequence, whereas excess of P and O was found for 3A + B and 4A + B, resulting in $AlP_{1.49}O_{5.26}$ and $AlP_{1.86}O_{6.50}$, respectively. With 2A + B SCs, the composition resembles stoichiometric $AlPO_4$ most closely ($AlP_{1.15}P_{4.34}$). Notably, the increase in P concentration from 3A to 4A cycles was only minimal (19.1 at% P to 19.7 at% P), underlining the presence of a saturation effect for higher numbers of P cycles. Hence, supercycles consisting of 1, 2, and 3A cycles with 1B cycle were further investigated in the following, with a focus on the effect of deposition temperature on the growth behavior and composition of the resulting films.

With all three schemes (A + B, 2A + B, 3A + B), the thickness was found to increase linearly with the number of supercycles between 50 and 250 (Fig. 7c). This was demonstrated by separate linear fits (shown in Fig. S6, with $R^2 > 0.999$), yielding GPSC values of 0.19 Å (A + B), 0.30 Å (2A + B), and 0.39 Å (3A + B), respectively. These are well in line with the values obtained from the initial variation of the number of A cycles. Additionally, the linear fits begin nearly at the origin, indicating that the growth is neither enhanced nor hindered during the nucleation period. A representative image of AlP_xO_y deposited uniformly on a 2-inch Si wafer using 250 3A + B SCs at 150 °C is depicted in Fig. S7. Lastly, the temperature dependence of the three SC schemes was investigated by varying the substrate temperature from 60 to 240 °C (Fig. 7d), the upper limit of the employed reactor setup. For the A + B sequence, the GPSC remained stable over the entire temperature range, whereas the 2A + B sequence showed a slight, irregular increase in GPSC with increasing temperature. For the 3A + B sequence, on the other hand, the GPSC increased from 3.3 Å at 60 °C to 3.9 Å at 150 °C and then remained constant up to 240 °C. These findings suggest that the Al-cycle is relatively unaffected by the temperature, while the P-cycle is slightly enhanced at higher temperatures. Hence, the increase in growth is more pronounced, the more P cycles are employed in each SC. This is reflected in the increasing ratio of the P to Al peaks in the RBS spectra, as shown in Fig. 8 for the films obtained with the SC sequences A + B, 2A + B, and 3A + B at 150 °C. Comprehensive RBS/NRA data for the different SC sequences are provided in the SI (Tables S3–S10). The shift in composition is further quantified by the absolute areal density of O, P, and Al atoms measured by RBS (Fig. S8): the areal density of Al remains constant primarily for all three SC sequences, while the areal densities of P and O atoms are increasing with the temperature. This increase with temperature is steeper the more P-cycles are applied in the sequence.

The AlP_xO_y stoichiometry calculated from these RBS/NRA results (Fig. 9) shows that under-stoichiometric material is deposited with A + B sequences over the entire temperature range that was investigated, and P-rich material with 3A + B. When the 2A + B sequence is applied, stoichiometric $AlPO_4$

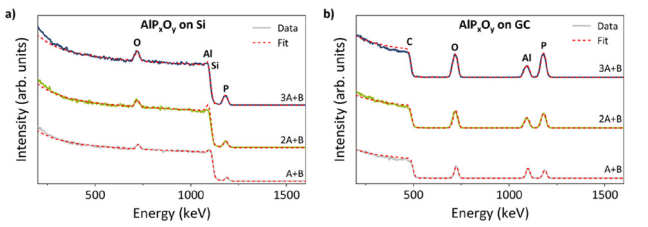

Fig. 8 RBS spectra of AlP_xO_y deposited at 150 °C using different PEALD SC sequences (bottom: A + B, middle: 2A + B, top: 3A + B) on (a) Si and (b) GC.

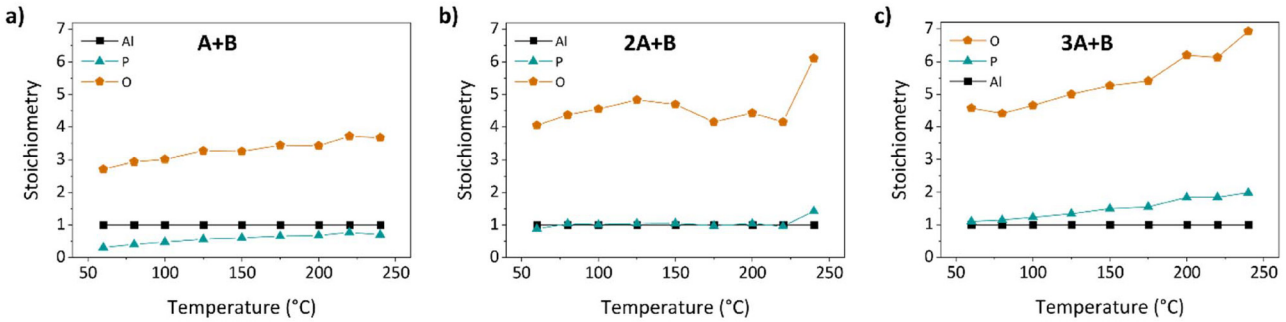

Fig. 9 Stoichiometry of AlP_xO_y thin films deposited on GC using supercycle sequences consisting of (a) one, (b) two, and (c) three $P(NMe_2)_3$ cycles and in each case one TMA cycle, as determined by RBS/NRA. For better visualization, P and O values have been normalized to an Al ratio of 1.

can be deposited over a wide temperature range from 60 °C to 220 °C. Only at 240 °C is a significant PO_x surplus observed. Overall, the achievement of $AlPO_4$ deposition at temperatures as low as 60 °C represents a considerable improvement compared to the 125 °C from prior work by Blomme *et al.*[37]

Analysis of representative films deposited with a 2A + B and 3A + B SC sequence on Si by X-ray diffraction (XRD) showed no reflections in a 2θ range of 5° to 60°, revealing an amorphous structure of the grown $AlPO_4$ (Fig. S9). This implies that the films are free of grain boundaries, which is beneficial for application as a protective layer.[19–21]

To investigate the behavior of the films at elevated temperatures, selected samples were annealed for 16 h at 600 °C under ambient conditions. Thereby, the film deposited with 150 3A + B SCs remained amorphous in XRD measurements (Fig. S9). This is in accordance with prior studies, which report an annealing temperature of around 900 °C to induce crystallization of $AlPO_4$.[35,37] For films deposited with the same sequence at 60 °C, 100 °C, and 200 °C, the areal densities of Al and P atoms determined by RBS on GC and Si were barely influenced by the annealing step, while the areal density of O in the 60 °C and 100 °C samples slightly increased, leading to an increased O-surplus (Table S11). Only one sample deposited with 2A + B SCs at 150 °C showed a decrease in P and O areal densities upon annealing, resulting in Al-rich material. The mechanism of this PO_x loss has not yet been explained and would require further annealing experiments, which exceed the scope of this study. Still, samples deposited with 3A + B SCs remained stable at 600 °C under ambient conditions, retaining their amorphous structure and showing no loss of phosphorus.

XPS analysis of AlP_xO_y thin films

Complementary to the analysis of the bulk composition by RBS/NRA, XPS was performed to get in-depth insights into the surface composition and chemical bonding states of the thin film surface upon applying different SC sequences at 150 °C. No signal was detected in the N 1s region, and the C 1s signal at 284.8 eV (ref. 64) can be attributed to adventitious carbon that is completely removed upon Ar^+ sputtering, as shown by a representative survey spectrum (Fig. S10). Hence, the films are impurity-free, consistent with the RBS/NRA results. Comparison of the Al 2p, P 2p, and O 1s peak positions across the different SC schemes reveals distinct changes in the deposited material's structure. As shown by the overlay in Fig. 10, the peak positions of the A + B sample are notably shifted towards lower binding energies, indicating the incorporation of Al_2O_3. Hence, a notable amount of Al–O–Al bonding is present, and the film can be instead characterized as a P-doped oxide.[37] For the 2A + B sample, a shift towards an accurate phosphate material with exclusive Al–O–P bonding[37] is observed with the following binding energies: 75.6 eV (Al 2p), 134.9 eV (P 2p), and 532.7 eV (O 1s). The peak positions of the 3A + B and 4A + B samples con-

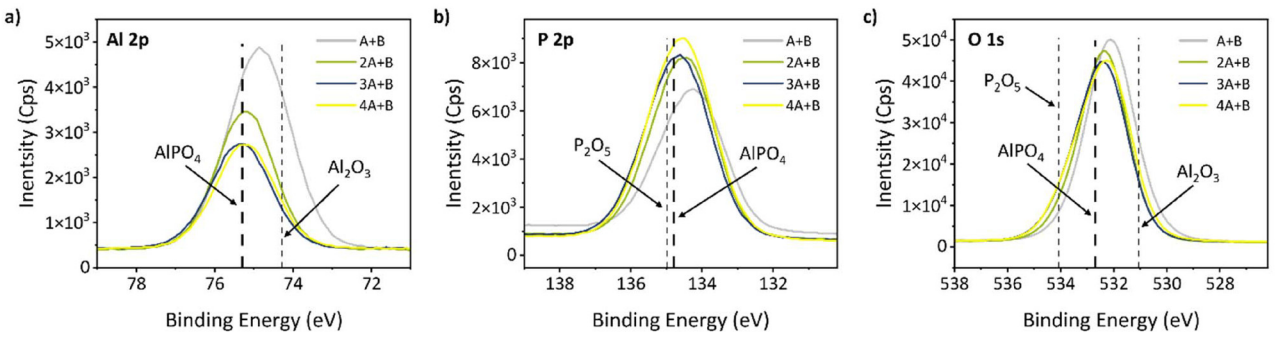

Fig. 10 Fitted data of (a) Al 2p, (b) P 2p, and (c) O 1s core level XPS spectra of as-introduced $AlPO_4$ thin films deposited on Si with 150 SCs at 150 °C and varying SC sequences. The dashed lines indicate the expected peak positions for $AlPO_4$,[68] P_2O_5,[72] and Al_2O_3.[73]

tinue to gradually move towards slightly higher binding energies (as summarized in Table S12), but overall, still closely resemble the expected positions,[65] including those previously reported for ALD-deposited $AlPO_4$.[22,37]

Nevertheless, there is a slight shoulder at higher binding energies of the P 2p and O 1s peaks with the 3A + B and 4A + B sequences. This was previously linked to contributions from a P–O–P bonding motif[37,69–71] and thus indicates the presence of P_2O_5 species, which is consistent with the P surplus observed in these films by RBS. Additionally, the core-level spectra peak shapes of the A + B sample differ significantly from the other sequences: the Al 2p peak is considerably broader, while the P 2p and O 1s peaks are asymmetric. Altogether, this clearly indicates the presence of two distinct species, aligning well with the conclusions drawn from the peak positions.

As the binding energies of the different species are very close to each other, it is not possible to reliably deconvolute the individual species. Yet, the shares obtained from fits of the complete Al 2p, P 2p, and O 1s components follow these trends: the Al content decreases, and the P content increases with the number of P-cycles. Overall, the XPS results align well with the RBS/NRA analysis, underscoring the importance of closely controlling the deposition parameters to achieve the desired bonding structure. It is confirmed that (at 150 °C) the 2A + B sequence is best suited to obtain stoichiometric $AlPO_4$ films with proper phosphate bonding.

Morphological characterization: AFM and TEM

The morphology and microstructure of selected AlP_xO_y thin films were investigated using atomic force microscopy (AFM) and transmission electron microscopy (TEM). Using AFM, samples deposited at 60 °C, 150 °C, and 240 °C with each A + B, 2A + B, and 3A + B SC sequences were analyzed to gain insight into the influence of deposition temperature and composition on the surface features and roughness of the thin films. Exemplarily, the images of samples deposited with 3A + B SCs are shown in Fig. 11, and the further AFM images, as well as 3D depictions, are included in the SI (Fig. S11–S15).

With all parameters, highly smooth films are obtained with root-mean-square roughness (R_{RMS}) values in the range of 0.2 nm (see Table 3). The only outliers are the films deposited with a 2A + B sequence at 150 °C and 240 °C, which exhibit increased R_{RMS} values of 0.74 nm and 0.45 nm, respectively. Nevertheless, the process provides a uniform and conformal coating, with R_{RMS} values below that of the underlying Si wafer (roughness of ~1 nm)[74] for all deposition conditions.

Table 3 Roughness values of AlP_xO_y samples deposited with 150 SCs with different sequences and temperatures, as determined by AFM with the respective XRR thicknesses

SC sequence	Temperature (°C)	Thickness (nm)	R_{RMS} (nm)
A + B	60	28.0	0.16
A + B	150	28.2	0.22
A + B	240	27.5	0.17
2A + B	60	41.0	0.24
2A + B	150	42.7	0.74
2A + B	240	41.4	0.45
3A + B	60	49.5	0.23
3A + B	150	58.7	0.25
3A + B	240	58.0	0.18
4A + B	150	68.8	0.22

As the 2A + B SC sequence delivered stoichiometric $AlPO_4$ thin films, these layers were further investigated by high-resolution transmission electron microscopy (HRTEM). To examine the influence of deposition temperature on the film's microstructure and interface, films deposited at 60 °C, 150 °C, and 240 °C were inspected (Fig. 12). As expected from the similar atomic numbers of $AlPO_4$, the underlying Si substrate with its native oxide, and the protective carbon layer, the contrast in the TEM images is relatively poor.[75] Notably, the transition from the native SiO_2 to $AlPO_4$ is challenging to observe. To improve the contrast, the 240 °C sample was sputtered with Au as a protective layer. While this enhanced the contrast, a comparably rough interface was observed at the top of the $AlPO_4$ layer, likely due to an unexpected reaction with the sputtered Au. Nonetheless, this sample demonstrates a sharp interface with the underlying substrate, despite the possibility that the O_2 plasma may oxidize the Si substrate during the initial PEALD cycles.

Despite the unfavorable contrast, it is evident that dense, defect-free AlP_xO_y thin films were deposited at all deposition temperatures. Higher magnification (Fig. S16, bottom row) revealed the absence of an ordered lattice, indicating the amorphous nature of the films. Unfortunately, this also led to even

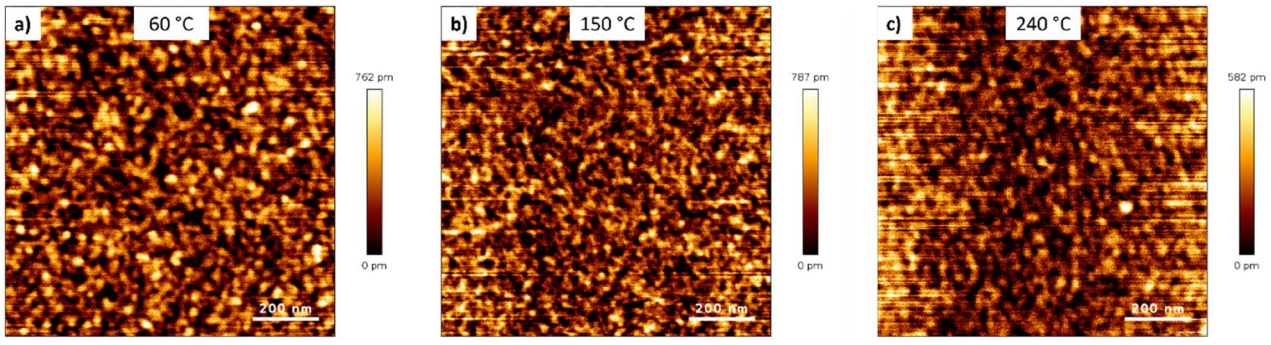

Fig. 11 AFM images of AlP_xO_y deposited on Si with 150 3A + B supercycles at (a) 60 °C, (b) 150 °C, and (c) 240 °C.

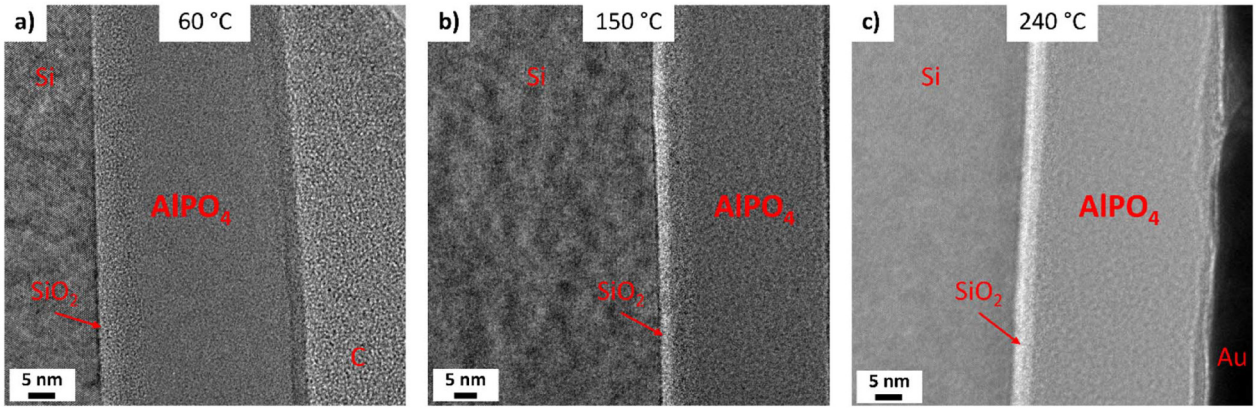

Fig. 12 Cross-section HRTEM images of $AlPO_4$ deposited on Si with 150 2A + B supercycles at (a) 60 °C, (b) 150 °C, and (c) 240 °C.

weaker contrast, preventing a more detailed examination of the thin film interface. On the other hand, overview scanning TEM (STEM) images (Fig. S16, top row) revealed an even, conformal coating over the entire scanning area.

Motivated by the high quality of the films and the ALD-typical conformality, we deposited an $AlPO_4$ thin film using 10 supercycles of the 2A + B sequence at 150 °C. According to the GPSC obtained from the linearity, this is expected to yield a thickness of around 3.0 nm. The sample was analyzed by an overview STEM image and HRTEM images, as depicted in the SI (Fig. S17). The poor contrast prevents us from distinguishing between the native oxide and the $AlPO_4$ film, but the visually determined thickness of approximately 4.5 nm closely matches the expected combined value. Additionally, the film remains uniform and defect-free, which is promising for further downscaling to achieve the required thickness for bilayer $AlPO_4$.

To conclude the SC approach, we demonstrated the growth of pure, smooth AlP_xO_y over a wide temperature range from 60 °C to 240 °C, with the GPSC remaining relatively unaffected by the deposition temperature. P and O contents were found to increase primarily with the number of PO_x cycles and secondarily with the temperature, and there is no indication that growth at even lower or higher temperatures would be impracticable. Further increasing the temperature would require a different reactor setup capable of heating above 240 °C, but could open up further possibilities to tune the materials' composition, *e.g.*, allow the deposition of stoichiometric $AlPO_4$ with an A + B scheme when the observed trend is extrapolated. In the temperature regime investigated, the composition of the resulting films can be readily tuned incrementally from $AlP_{0.31}O_{2.72}$ (P/Al = 0.31, A + B at 60 °C) to $AlP_{1.98}O_{6.93}$ (P/Al = 1.98, 3A + B at 240 °C) by adjusting the SC scheme and deposition temperature accordingly. The PO_x content of the film could be further enhanced by employing more than three A cycles or using higher temperatures. Likewise, the Al_2O_3 content could be increased using a supercycle scheme with multiple B cycles. This tunability provides broad variability and enables precise tailoring of the material to specific applications.

In comparison to the related process reported by Hornsveld and co-workers with $PO(OMe)_3$,[22] the incorporation of PO_x was facilitated. This could be explained by an enhanced reactivity of the P–N bonds in $P(NMe_2)_3$ towards the O_2 plasma and less steric hindrance of the employed P^{3+} precursor. Our results align well with those recently reported by Blomme *et al.*, who also employed supercycles of $P(NMe_2)_3$–O_2 plasma and TMA–O_2 plasma.[37] Nonetheless, we could demonstrate $AlPO_4$ growth at even lower deposition temperatures (60 °C compared to 125 °C) with a more precise control of the AlP_xO_y composition and fewer PO_x cycles required in the SC sequence to achieve stoichiometric $AlPO_4$. Furthermore, significantly shorter precursor and plasma lengths as well as purge durations were sufficient for saturation. This drastically reduces processing times, and shorter plasma pulses are especially beneficial for preventing modifications to the substrate and the interface with the film. Interestingly, Blomme and co-workers did not see an influence on the GPSC when employing just one PO_x sub-cycle (at 300 °C)[37] compared to a typical growth per cycle (GPC) of 1.3 Å for a TMA–O_2 plasma process,[76] while we observed an enhanced GPSC of 1.9 Å with the same sequence at 150 °C. Additionally, we did not see a decrease in GPSC with the temperature (as observed by Blomme *et al.* between 125 °C and 350 °C) but instead, the GPSC remained constant or slightly increased from 60 °C to 240 °C. These distinctions could be explained by varying reactor setups and plasma configurations, stressing the need for careful process optimization and adaption to the specific reactor design. Specifically, Blomme *et al.*[37] employed a remote plasma source, whereas our reactor features a direct plasma setup, which significantly influences the reactive plasma species that reach the substrate and explains the considerably longer plasma exposure time of 10 s in the prior study.

Conclusion and outlook

In this extensive study, we compared two approaches to deposit $AlPO_4$ thin films by PEALD with O_2 plasma: a dual-

source process using a precursor containing both Al and P, and a supercycle process combining separate PO_x and Al_2O_3 cycles. For the first method, we synthesized **TMAPET** and the new **TMAPIP**, which include phosphorus species adducted to TMA. Our DFT calculations show similar stability for both adducts with either alkyl group. However, only **TMAPIP** can be volatilized intact within a suitable temperature range for evaporation, making it an ideal dual-source precursor candidate. Despite its promising thermal properties and simpler process design, this approach yielded films with a maximum P content of only a few atomic percent, suggesting a reaction mechanism involving the release of the P adduct. In summary, although this approach was not effective in achieving stoichiometric $AlPO_4$ films, it offers a pathway to deposit intrinsically P-doped Al_2O_3 thin films.

In the second approach, we employed a supercycle procedure using TMA as the Al precursor and $P(NMe_2)_3$ as the P precursor, which possesses suitable thermal properties. A simplified gas-phase model of $P(NMe_2)_3$ interacting with $Al(OH)_3$ to simulate the reactive surface species post the TMA–O_2 plasma sub-cycle demonstrates that the formation of a P–O bond is favorable upon the release of $HNMe_2$. Employing a 1 : 1 ratio of the PO_x and Al_2O_3 sub-cycles already yielded near-stoichiometric AlP_xO_y films. An increase in the number of PO_x cycles per supercycle led to stochiometric $AlPO_4$ (2A + B) and, subsequently, to PO_4-rich films (3A + B). Consequently, a 2A + B sequence can be considered appropriate to deposit stochiometric $AlPO_4$ thin films, whereas the other sequences are to be chosen to obtain non-stoichiometric compositions deliberately. The ALD-typical linear growth has been demonstrated for each sequence with mostly constant GPSC values across the entire temperature range, allowing the film composition to be fine-tuned by the deposition temperature. The films were found to be highly smooth, with R_{RMS} values in the range of 0.2 nm, irrespective of the process parameters. TEM confirmed a smooth surface and revealed dense, defect-free, closed layers. To achieve 2D $AlPO_4$, initial downscaling experiments were conducted by depositing a sample with 10 SCs (2A + B) and an expected thickness of 3.0 nm. With these parameters, a closed thin film was already achieved, providing a strong foundation for experimental exploration of $AlPO_4$ as a 2D material. In the future, we will further downscale the layers to experimentally demonstrate the bilayer structure and advance 2D $AlPO_4$ from theory to functional devices.

Experimental

Precursor synthesis

Handling of air- and moisture-sensitive compounds was carried out in a glove box (MBraun). All syntheses were conducted in oven-dried and degassed glassware under an argon atmosphere (AirLiquide, 99.995%) using conventional Schlenk techniques. Solvents were purified and dried using an MBraun-SPS-800 purification system. TMA is highly pyrophoric and must be handled with appropriate precautions to prevent any hazards arising from contact with air. $P(NMe_2)_3$ (97%) was purchased from Sigma-Aldrich and used as received without further purification.

Synthesis of trimethylaluminum triethylphosphine (TMAPET)

TMAPET was synthesized by dissolving triethylphosphine (4.0 g, 33.9 mmol) in Et_2O (20 mL) and adding TMA (2.4 g, 33.9 mmol) dropwise. The mixture was stirred for 3 h, and the solvent was removed under reduced pressure. The crude product was distilled at 60 °C under reduced pressure (approx. 5×10^{-2} mbar), giving **TMAPET** as a colorless liquid (6.1 g, 32.1 mmol 94%). ^{1}H NMR (300 MHz, C_6D_6): δ (ppm) = 1.03 (m, 6H, CH_2CH_3), 0.71 (m, 9H, CH_2CH_3), −0.33 (s, 9H, Al(CH_3)$_3$). ^{13}C NMR (75 MHz, C_6D_6): δ (ppm) = 13.35 (d, J = 15.1 Hz, 3C, CH_2CH_3), 7.55 (s, 3C, CH_2CH_3), −8.21 (s, 3C, Al(CH_3)$_3$).

Synthesis of trimethylaluminum triisopropylphosphine (TMAPIP)

TMAPIP was synthesized analogously, using triisopropylphosphine (4.0 g, 25.0 mmol) in Et_2O (20 mL) with dropwise addition of TMA (1.8 g, 25.0 mmol). The crude product was purified by sublimation at 68 °C under reduced pressure (approx. 5×10^{-2} mbar), giving **TMAPIP** as a colorless solid (5.5 g, 22.7 mmol 94%). ^{1}H NMR (300 MHz, C_6D_6): δ (ppm) = 1.73 (dq, J = 14.5, 7.3 Hz, 3H, $CH(CH_3)_2$), 0.91 (dd, J = 13.2, 7.2 Hz, 18H, $CH(CH_3)_2$), −0.26 (s, 9H, Al(CH_3)$_3$). ^{13}C NMR (75 MHz, C_6D_6): δ (ppm) = 20.49 (d, J = 11.4 Hz, 3C, $CH(CH_3)_2$), 18.73 (d, J = 2.1 Hz, 6C, $CH(CH_3)_2$), −6.31 (s, 3C, Al(CH_3)$_3$). LIFDI-MS (m/z): [**TMAPIP**-H]$^+$: calc. 233.20, found 233.13.

Precursor characterization

Storage and sample preparation were carried out in an argon-filled glove box (MBraun LM 100). Deuterated C_6D_6, purchased from Millipore for NMR experiments, was degassed before use and stored over 4 Å molecular sieve. All NMR spectra were recorded on a Bruker Avance III 400 HD instrument and referenced to the internal solvent signal (C_6D_5H) and analyzed with the software MestReNova v14.2.1-27684 from Mestrelab Research S.L. LIFDI-MS measurements were carried out using a Jeol AccuTOF GCv (Freising, Germany) spectrometer, equipped with a LIFDI source from Linden CMS, Weyhe, Germany. TG and stepped iso-TG experiments of **TMAPET** and **TMAPIP** were conducted on a Netzsch STA-409 device, and TG of $P(NMe_2)_3$ was performed on a Hitachi NEXTA STA200 device. All TG experiments were run in a temperature range of 30 °C to 550 °C under a nitrogen atmosphere with standard sample sizes of ~10 mg–20 mg, a heating rate of 5 K min^{-1} and a nitrogen flow rate (AirLiquide, 99.999%) of 300 mL min^{-1} for the Netzsch device and of 200 mL min^{-1} for the Hitachi device. Vapor pressures were estimated from DTG data based on a procedure described in the literature,[58,59] using benzoic acid as the reference.

Thin film deposition

PEALD depositions of $AlPO_4$ were performed in a custom-built stainless-steel reactor (modular flow) for both the dual source and supercycle approach. The reactor chamber consists of a

square chamber (dimensions: 20 cm × 20 cm × 20 cm) with a viewport and a perpendicular top-flow (showerhead) geometry for precursor and gas delivery featuring a single-wafer (2-inch) grounded substrate holder located between the antennas. A direct electron cyclotron wave resonance O_2 plasma was generated by a radio-frequency generator (13.56 MHz) and an active magnetic flux density of 2.8 mT using a matching network with a plasma power of 100–300 W in the pressure range of 10^{-2}–10^{-3} mbar.[66] **TMAPIP**, $P(NMe_2)_3$, and TMA were filled into stainless-steel cartridges and maintained at 80 °C, 40 °C, and 0 °C, respectively. The plasma power was set to 200 W, whereas oxygen (Air Liquide, 99.995%) and argon (Air Liquide, 99.995%) gas flows were adjusted to 15 sccm for all depositions. CZ-Si(100) p-type wafers (MicroChemicals) with native oxide ($SiO_2 \approx 2$ nm) served as substrates for PEALD depositions and process optimization. The wafers were cleaned of dust by pressurized argon before usage. In RBS measurements, the Al signal overlaps with the Si substrate signal; therefore, depositions were also performed on GC substrates (~1 cm × 0.5 cm) that were cleaned by washing with isopropanol, ultrasonication in water, and subsequent blow-drying with pressurized argon. The C and N contents were then derived from the Si substrate, whereas the Al, O, and P contents were derived from the GC substrate.

Thin film characterization

The thickness and density of AlP_xO_y films were determined by X-ray reflectometry (XRR; Bruker D8 Discover XRD) with Cu-K_α radiation (λ = 1.5418 Å) in θ–2θ locked coupled mode. 2θ was increased from 0.1° to 3° with a step size of 0.01° and a scan speed of 1 s. The composition of selected thin films on Si(100) and GC substrates was determined using two ion beam analytical methods at the 4 MV tandem accelerator facility RUBION at Ruhr University Bochum, with an incident tilt angle of 7° to the substrate. RBS was performed with a $^4He^+$ ion beam of 2.0 MeV (intensity 40–50 nA), enabling good quantification of the higher-Z elements (here, Al and P). To determine the O content and detect C and N contaminations with high sensitivity, nuclear reaction analysis (NRA) was performed using a 1.0 MeV deuteron beam. For RBS, a silicon detector was used for the backscattered He-nuclei at an angle of 160°, while for NRA, the detection angle for the emitted protons was 135°. The SIMNRA program[77] was employed for the processing and analysis of RBS and NRA raw data. XPS studies were conducted on a PHI 5600 instrument using Al-K_α photon radiation (1486.6 eV). Selected AlP_xO_y thin film samples were analyzed by a combination of survey and core-level scans for peaks of interest. Step widths were adjusted to 0.5 eV for each survey scan and 0.05 eV for the core level scans. Hereby, the pass energies were adjusted to 187.5 eV and 29.35 eV, respectively. All binding energies of Al 2p, P 2p, and O 1s were referenced to the signal of adventitious carbon species (284.8 eV).[67] The analysis chamber pressure was maintained at $<10^{-7}$ mbar. Recordings were taken of the as-introduced surface, followed by scans after an Ar^+-sputter step (2 min, 3 kV, 2 × 2), and the as-introduced surfaces were analyzed for chemical species. The deconvolution analysis was completed using Shirley background processing and Gaussian functions in Casa XPS software.[78] AFM measurements of selected samples were conducted on a JPK NanoWizard 3 device equipped with an anti-vibration box in tapping mode using a Multi75GD-G cantilever. Images were recorded at a line-scan rate of 1 Hz and a resolution of 512 × 512 pixels in a scan range of 1 μm × 1 μm. Recorded images were processed with JPK Data Processing software by subtracting a polynomial fit from each scan line and, wherever necessary, replacing outliers. The images were analyzed using Gwyddion software[79] to determine the RMS roughness of the films. TEM was carried out on a Tecnai F30 device (FEI) operated at 300 kV and equipped with a high-angle annular dark field detector for scanning imaging and an energy dispersive X-ray spectrometer (EDXS) (TEAM Octane T Optima EDS windowless, Edax/Ametek). Cross sections of the specimens were prepared for TEM using a dual-beam focused ion beam (FIB) microscope (Helios 5 CX, TFS) operated at 30 kV. As a final specimen preparation step 5 kV ion beam cleaning was applied to the TEM sample to reduce damage by the FIB process. Cross-section images of the specimens were recorded using bright-field high-resolution TEM. Cross-section images of the specimens were recorded using bright-field high-resolution TEM.

Density functional theory calculations

The TURBOMOLE software suite was used for all density functional theory (DFT) calculations.[80,81] The calculations used the hybrid exchange–correlation functional PBE0, with an m3 integration grid.[82,83] The orbitals for all atoms were expressed using the all-electron triple zeta valence basis set def2-TZVP.[84,85] The convergence criteria for the electronic SCF cycles were 10^{-6} Ha. Geometry optimization was performed using internal redundant coordinates and the convergence criterion of the energy gradients is less than 10^{-3} Ha The adduct formation energy is calculated as the energy difference between the adduct and the sum of the energies of isolated TMA and PET/PIP (eqn (1)).

$$\Delta_{add}E = E_{TMAPET/TMAPIP} - (E_{TMA} + E_{PET/PIP}) \quad (1)$$

The interaction energy, $\Delta_{ALD}E$, of $P(NMe_2)_3$ and $Al(OH)_3$, releasing $HN(Me)_2$, as a simplified gas phase model for the ALD chemistry, are calculated similarly from eqn (2):

$$\Delta_{ALD}E = E_{P(NMe_2)_2\text{-}Al(OH)_2} + E_{HNMe_2} - (E_{P(NMe_2)_3} + E_{Al(OH)_3}) \quad (2)$$

Conflicts of interest

There are no conflicts to declare.

Data availability

The data supporting this article have been included as part of the supplementary information (SI). Supplementary information: ^1H

and ^{13}C NMR spectra, vapor pressure graphs, LIFDI-MS spectrum, RBS/NRA data, PEALD process development details, XRD pattern, XPS survey spectra and data, AFM images, and TEM images. See DOI: https://doi.org/10.1039/d5dt02282g.

Acknowledgements

This work was funded by the German Research Foundation (PHANTOM, project nr. 496964156). AD thanks the Leibniz Association (ASPIRE-2D project nr. P155/2023) and the Fraunhofer Society (Attract project grant nr. Attract 40-00643) for supporting this work. The work of KR was funded by Research Ireland, formerly the Irish Research Council, under award number GOIPD/2023/1099 and by the Bengt Lundqvist's Memory Foundation. MN was supported by the European Commission through the ASCENT+: Access to European Infrastructure for Nanoelectronics project, funded under Horizon Europe, grant 871130.

References

1 P. Patnaik, *Handbook of inorganic chemicals*, McGraw-Hill, New York, NY, 2003.
2 S. Yan, Y. Xue, Y. Yang, X. Qi, L. Song and Y. Sun, *J. Appl. Polym. Sci.*, 2017, **134**, 45542.
3 N. Li, M. Zhong, Z. Xu and Z. Zhang, *Mater. Lett.*, 2018, **213**, 335–337.
4 H. Li, Z. Zheng, S. Liu, Z. Zhao, Y. Yan and X. Wang, *J. Am. Ceram. Soc.*, 2024, **107**, 1871–1882.
5 S. T. Wilson, B. M. Lok, C. A. Messina, T. R. Cannan and E. M. Flanigen, *J. Am. Chem. Soc.*, 1982, **104**, 1146–1147.
6 N. Rajic, *J. Serb. Chem. Soc.*, 2005, **70**, 371–391.
7 B. Kim, C. Kim, T.-G. Kim, D. Ahn and B. Park, *J. Electrochem. Soc.*, 2006, **153**, A1773.
8 B. Xiao, B. Wang, J. Liu, K. Kaliyappan, Q. Sun, Y. Liu, G. Dadheech, M. P. Balogh, L. Yang, T.-K. Sham, R. Li, M. Cai and X. Sun, *Nano Energy*, 2017, **34**, 120–130.
9 S. Deng, B. Xiao, B. Wang, X. Li, K. Kaliyappan, Y. Zhao, A. Lushington, R. Li, T.-K. Sham, H. Wang and X. Sun, *Nano Energy*, 2017, **38**, 19–27.
10 S. Knohl, A. K. Roy, R. Lungwitz, S. Spange, T. Mäder, D. J. Nestler, B. Wielage, S. Schulze, M. Hietschold, H. Wulff, C. A. Helm, F. Seidel, D. R. T. Zahn and W. A. Goedel, *ACS Appl. Mater. Interfaces*, 2013, **5**, 6161–6167.
11 C. R. Maier and L. E. Jones, *Carbon*, 2005, **43**, 2272–2276.
12 J. Liu, Y. Tang, B. Xiao, T.-K. Sham, R. Li and X. Sun, *RSC Adv.*, 2013, **3**, 4492.
13 A. S. M. M. Reza, M. A. Afzal and S. H. Naqib, *Mater. Sci. Semicond. Process.*, 2025, **190**, 109322.
14 S. T. Meyers, J. T. Anderson, D. Hong, C. M. Hung, J. F. Wager and D. A. Keszler, *Chem. Mater.*, 2007, **19**, 4023–4029.
15 J. H. Morris, P. G. Perkins, A. E. A. Rose and W. E. Smith, *Chem. Soc. Rev.*, 1977, **6**, 173–194.
16 F. S. Sayyedan and M. H. Enayati, *Surg. Eng.*, 2019, **35**, 670–676.
17 F. Gutiérrez-Mora, K. C. Goretta, D. Singh, J. L. Routbort, S. Sambasivan, K. A. Steiner, J. Adabie and K. K. Rangan, *J. Eur. Ceram. Soc.*, 2006, **26**, 1179–1183.
18 E. Valenzuela-Heeger, J. Binner, S. Butterworth and C. Hawkins, *Ceram. Int.*, 2025, **51**, 38579–38590.
19 M.-A. Nicolet, *Thin Solid Films*, 1978, **52**, 415–443.
20 M. Leskela, E. Salmi and M. Ritala, *Mater. Sci. Forum*, 2016, **879**, 1086–1092.
21 S. W. Park, G. D. Han, H. J. Choi, F. B. Prinz and J. H. Shim, *Appl. Surf. Sci.*, 2018, **441**, 718–723.
22 N. Hornsveld, W. M. M. Kessels and M. Creatore, *J. Phys. Chem. C*, 2020, **124**, 5495–5505.
23 S. M. George, *Chem. Rev.*, 2010, **110**, 111–131.
24 V. Cremers, R. L. Puurunen and J. Dendooven, *Appl. Phys. Rev.*, 2019, **6**, 021302.
25 D. R. Boris, V. D. Wheeler, N. Nepal, S. B. Qadri, S. G. Walton and C. R. Eddy, *J. Vac. Sci. Technol., A*, 2020, **38**, 040801.
26 F. Preischel, D. Zanders, T. Berning, A. Kostka, D. Rogalla, C. Bock and A. Devi, *Adv. Mater. Interfaces*, 2023, **10**, 2300244.
27 E. I. Altman, *J. Phys. Chem. C*, 2017, **121**, 16328–16341.
28 D. Naberezhnyi, L. Mai, N. Doudin, I. Ennen, A. Hütten, E. I. Altman, A. Devi and P. Dementyev, *Nano Lett.*, 2022, **22**, 1287–1293.
29 P. Dementyev, N. Khayya, D. Zanders, I. Ennen, A. Devi and E. I. Altman, *Small*, 2023, **19**, e2205602.
30 M. Tiitta, E. Nykänen, P. Soininen, L. Niinistö, M. Leskelä and R. Lappalainen, *Mater. Res. Bull.*, 1998, **33**, 1315–1323.
31 M. Nieminen, L. Niinist and R. Lappalainen, *Mikrochim. Acta*, 1995, **119**, 13–22.
32 J. Hämäläinen, J. Holopainen, F. Munnik, M. Heikkilä, M. Ritala and M. Leskelä, *J. Phys. Chem. C*, 2012, **116**, 5920–5925.
33 A. J. M. Mackus, J. R. Schneider, C. MacIsaac, J. G. Baker and S. F. Bent, *Chem. Mater.*, 2019, **31**, 1142–1183.
34 K. B. Kvamme, A. Ruud, K. Weibye, T. Sajavaara and O. Nilsen, *J. Vac. Sci. Technol., A*, 2021, **39**, 032404.
35 T. Dobbelaere, A. K. Roy, P. Vereecken and C. Detavernier, *Chem. Mater.*, 2014, **26**, 6863–6871.
36 J. Su, T. Tsuruoka, T. Tsujita, Y. Nishitani, K. Nakura and K. Terabe, *Chem. Mater.*, 2019, **31**, 5566–5575.
37 R. Blomme, A. Chalishazar, L. Henderick, F. Munnik, J. Meersschaut, M. M. Minjauw, C. Detavernier and J. Dendooven, *J. Vac. Sci. Technol., A*, 2025, **43**, 022409.
38 I. M. Germaine and L. McElwee-White, *Cryst. Growth Des.*, 2024, **24**, 1–16.
39 G. Karmakar, A. Tyagi and A. Y. Shah, *Coord. Chem. Rev.*, 2024, **504**, 215665.
40 C. G. Lugmair, T. D. Tilley and A. L. Rheingold, *Chem. Mater.*, 1999, **11**, 1615–1620.
41 J. M. Gaskell, S. Przybylak, A. C. Jones, H. C. Aspinall, P. R. Chalker, K. Black, R. J. Potter, P. Taechakumput and S. Taylor, *Chem. Mater.*, 2007, **19**, 4796–4803.

42 J.-H. Kim, T. T. Ngoc Van, J. Oh, S.-M. Bae, S. I. Lee, B. Shong and J.-H. Hwang, *Ceram. Int.*, 2020, **46**, 10121–10129.
43 J. Harjuoja, T. Hatanpää, M. Vehkamäki, S. Väyrynen, M. Putkonen, L. Niinistö, M. Ritala, M. Leskelä and E. Rauhala, *Chem. Vap. Deposition*, 2005, **11**, 362–367.
44 E. Østreng, H. H. Sønsteby, S. Øien, O. Nilsen and H. Fjellvåg, *Dalton Trans.*, 2014, **43**, 16666–16672.
45 M. B. Smith, *J. Organomet. Chem.*, 1972, **46**, 31–49.
46 P. Maue, É. Chantraine, F. Pieck and R. Tonner-Zech, *Chem. Mater.*, 2025, **37**, 975–988.
47 A. R. Barron, *J. Chem. Soc., Dalton Trans.*, 1988, 3047.
48 C. H. Henrickson, D. Duffy and D. P. Eyman, *Inorg. Chem.*, 1968, **7**, 1047–1051.
49 A. Kuczkowski, S. Schulz, M. Nieger and P. R. Schreiner, *Organometallics*, 2002, **21**, 1408–1419.
50 D. A. Wierda and A. R. Barron, *Polyhedron*, 1989, **8**, 831–834.
51 L. Brieger, A. Hermann, C. Unkelbach and C. Strohmann, *Acta Crystallogr., Sect. E: Crystallogr. Commun.*, 2018, **74**, 267–270.
52 X. Chen, Y. Zheng, Y. Chen, Y. Xu, F. Zhong, W. Zhang, Y. Xiao and Y. Zheng, *Int. J. Hydrogen Energy*, 2019, **44**, 27772–27783.
53 M. Acikgoz, M. R. Khoshi, J. Harrell, A. Genova, R. Chawla, H. He and M. Pavanello, *Phys. Chem. Chem. Phys.*, 2019, **21**, 15080–15088.
54 W. McFarlane, *Chem. Commun.*, 1967, 58.
55 H. J. Jakobsen, *J. Mol. Spectrosc.*, 1971, **38**, 243–251.
56 N. N. Korneev, I. M. Khrapova, A. V. Polonskii, N. I. Ivanova, A. V. Kisin and V. S. Kolesov, *Russ. Chem. Bull.*, 1993, **42**, 1390–1395.
57 Sigma-Aldrich Co., LLC., *Triethylphosphine – Safety Data Sheet*, available at: https://www.sigmaaldrich.com/DE/en/sds/aldrich/245275?userType=anonymous, accessed 21 May 2025.
58 G. V. Kunte, S. A. Shivashankar and A. M. Umarji, *Meas. Sci. Technol.*, 2008, **19**, 25704.
59 M. B. E. Griffiths, Z. S. Dubrawski, G. Bačić, A. Japahuge, J. D. Masuda, T. Zeng and S. T. Barry, *Eur. J. Inorg. Chem.*, 2019, **2019**, 4927–4938.
60 I. Langmuir, *Phys. Rev.*, 1913, **2**, 329–342.
61 D. Zanders, J. D. Masuda, B. Lowe, S. Curtis, A. Devi and S. T. Barry, *Z. Anorg. Allg. Chem.*, 2022, **648**, e202200249.
62 J. P. McCullough, J. F. Messerly, R. T. Moore and S. S. Todd, *J. Phys. Chem.*, 1963, **67**, 677–679.
63 J. H. Gross, *Eur. J. Mass Spectrom.*, 2020, **26**, 241–273.
64 N. F. Eisele, *Electrospray-Ionization Mass Spectrometry for the Analysis and Quantification of Carbanions*, Georg-August University, 2023.
65 V. E. Strempel, D. Löffler, J. Kröhnert, K. Skorupska, B. Johnson, R. N. d'Alnoncourt, M. Driess and F. Rosowski, *J. Vac. Sci. Technol., A*, 2016, **34**, 01A135.
66 M. Gebhard, L. Mai, L. Banko, F. Mitschker, C. Hoppe, M. Jaritz, D. Kirchheim, C. Zekorn, T. de Los Arcos, D. Grochla, R. Dahlmann, G. Grundmeier, P. Awakowicz, A. Ludwig and A. Devi, *ACS Appl. Mater. Interfaces*, 2018, **10**, 7422–7434.
67 T. L. Barr and S. Seal, *J. Vac. Sci. Technol., A*, 1995, **13**, 1239–1246.
68 D. Hasha, L. Sierra de Saldarriaga, C. Saldarriaga, P. E. Hathaway, D. F. Cox and M. E. Davis, *J. Am. Chem. Soc.*, 1988, **110**, 2127–2135.
69 L. Henderick, R. Blomme, M. Minjauw, J. Keukelier, J. Meersschaut, J. Dendooven, P. Vereecken and C. Detavernier, *Dalton Trans.*, 2022, **51**, 2059–2067.
70 G. D. Khattak, M. A. Salim, A. S. Al-Harthi, D. J. Thompson and L. E. Wenger, *J. Non-Cryst. Solids*, 1997, **212**, 180–191.
71 A. C. Kozen, A. J. Pearse, C.-F. Lin, M. Noked and G. W. Rubloff, *Chem. Mater.*, 2015, **27**, 5324–5331.
72 Y. Wang and P. M. A. Sherwood, *Surf. Sci. Spectra*, 2002, **9**, 159–165.
73 J. A. Rotole and P. M. A. Sherwood, *Surf. Sci. Spectra*, 1998, **5**, 18–24.
74 MicroChemicals GmbH, *Herstellung und Spezifikation von Silcium-Wafern*, available at: https://www.microchemicals.com/dokumente/anwendungshinweise/silizium_wafer_herstellung_spezifikationen.pdf, accessed 27 May 2025.
75 S. Yamashita, J. Kikkawa, K. Yanagisawa, T. Nagai, K. Ishizuka and K. Kimoto, *Sci. Rep.*, 2018, **8**, 12325.
76 J. L. van Hemmen, S. B. S. Heil, J. H. Klootwijk, F. Roozeboom, C. J. Hodson, M. C. M. van de Sanden and W. M. M. Kessels, *J. Electrochem. Soc.*, 2007, **154**, G165.
77 M. Mayer, *SIMNRA User's Guide.*, Report IPP 9/113, available at: https://mam.home.ipp.mpg.de/Report%20IPP%209-113.pdf, accessed 21 May 2025.
78 N. Fairley, V. Fernandez, M. Richard-Plouet, C. Guillot-Deudon, J. Walton, E. Smith, D. Flahaut, M. Greiner, M. Biesinger, S. Tougaard, D. Morgan and J. Baltrusaitis, *Appl. Surf. Sci. Adv.*, 2021, **5**, 100112.
79 D. Nečas and P. Klapetek, *Open Phys.*, 2012, **10**, 181–188.
80 *TURBOMOLE GmbH, TURBOMOLE. a Development of University of Karlsruhe and Forschungszentrum Karlsruhe GmbH*, 2020.
81 S. G. Balasubramani, G. P. Chen, S. Coriani, M. Diedenhofen, M. S. Frank, Y. J. Franzke, F. Furche, R. Grotjahn, M. E. Harding, C. Hättig, A. Hellweg, B. Helmich-Paris, C. Holzer, U. Huniar, M. Kaupp, A. Marefat Khah, S. Karbalaei Khani, T. Müller, F. Mack, B. D. Nguyen, S. M. Parker, E. Perlt, D. Rappoport, K. Reiter, S. Roy, M. Rückert, G. Schmitz, M. Sierka, E. Tapavicza, D. P. Tew, C. van Wüllen, V. K. Voora, F. Weigend, A. Wodyński and J. M. Yu, *J. Chem. Phys.*, 2020, **152**, 184107.
82 J. P. Perdew, K. Burke and M. Ernzerhof, *Phys. Rev. Lett.*, 1996, **77**, 3865–3868.
83 C. Adamo and V. Barone, *J. Chem. Phys.*, 1999, **110**, 6158–6170.
84 F. Weigend, *Phys. Chem. Chem. Phys.*, 2006, **8**, 1057–1065.
85 F. Weigend and R. Ahlrichs, *Phys. Chem. Chem. Phys.*, 2005, **7**, 3297–3305.